International Journal of Mechanical Sciences 2013, 66C(260-272)

Influence of Process Parameters on Grain Refinement in AA1050 Aluminum During Cold Rolling

Håkan Hallberg*
Division of Solid Mechanics
Lund University, Box 118, S-221 00 Lund, Sweden

Abstract

The microstructure evolution during cold rolling of commercial purity AA1050 aluminum is investigated through numerical simulations. A finite strain elasto-viscoplastic constitutive model is employed, where the dislocation density and average grain size are taken as variables characterizing the deformed microstructure. Grain size evolution due to dynamic recrystallization is considered and the microstructure quantities are allowed to influence the macroscopic material behavior in terms of the flow stress and deformation-rate dependence. The effects of such process parameters as rolling friction, thickness reduction in each rolling pass and amount of rolling asymmetry are discussed. The results indicate that grain refinement due to dynamic recrystallization is most significantly affected by the amount of thickness reduction in each pass and the level of rolling friction and to a lesser extent by the asymmetry of the rolling process. An increasing degree of asymmetry will, however, reduce the variations in grain size through the sheet thickness and leave the material more homogeneously recrystallized.

Keywords: Recrystallization, Grain size, Simulation, Cold rolling, Severe plastic deformation, Aluminum

1 Introduction

The grains in the microstructure of metallic materials largely dictate the macroscopic material behavior. Important mechanical properties such as ductility, strength and hardness can be related to the morphology of the microstructure and in particular to the size of

*Mail: hakan.hallberg@solid.lth.se. Tel.: +46 46 222 90 92. Fax: +46 46 222 31 15.

DOI: 10.1016/j.ijmecsci.2012.11.016

the grains. The grain size dependence is also significant regarding the material's resistance against wear and corrosion and for properties such as electrical end thermal conductivity. Grain sizes may evolve due to recrystallization whereby the internal energy level of the material, i.e. the grain boundary energy and the stored energy, is lowered. This energy reduction occurs by migration of high-angle grain boundaries and by the nucleation and growth of new and relatively dislocation-free grains.

Recrystallization might be a relatively slow and temperature-driven, static, process or it can proceed due to macroscopic deformation of the material, i.e. through dynamic recrystallization. The nature of the dynamic recrystallization depends on the type of material under consideration. The recrystallization process in materials of low stacking-fault energy, such as copper, is mainly a discontinuous process where new grains nucleate at sites in the microstructure that have enough stored energy [1]. In materials of higher stacking-fault energy, such as aluminum, dynamic recovery processes limit discontinuous dynamic recrystallization in favor of a continuous process.

Transitions from discontinuous to continuous recrystallization in aluminum are discussed in [2, 3]. These investigations conclude that in the presence of a significant fraction of high-angle grain boundaries, the tendency is that aluminum recrystallizes through a continuous process. This is further promoted if the material contains large second-phase particles and inclusions or if the material is exposed to large deformations. The inclination towards continuous recrystallization is also noted in [4, 5] for commercial purity aluminum.

Continuous dynamic recrystallization proceeds by the creation of subgrains from dislocation cells. With increasing macroscopic deformation, the subgrains gain enough crystallographic misorientation to eventually form new and separate grains in the microstructure. During progressing macroscopic deformation of the material, a certain incubation period is thus needed for the new grains to appear, a period during which high-angle boundaries are generated and new grains become distinguishable.

The production of very fine-grained materials, with grain sizes down to the nano-scale, has gained increasing interest in recent years. As mentioned initially, important mechanical, thermal and electrical properties of the material can be controlled through the grain size. Applications range from biomedical applications and micro-electro-mechanical systems (MEMS) to manufacturing of functionally graded materials and structural elements in the automotive and aeronautic industries. Weight reduction, tailored material properties as well as lowered fuel consumption and reduced emissions are obvious gains.

The present study concerns rolling of thin aluminum sheets where the grain microstructure becomes increasingly important as the sheet thickness is reduced. A sheet thickness reduced to the same order of magnitude as the grain size causes problems with deformation localization and fracture in the final sheet product, or even during the rolling process itself.

The thickness of the sheets frequently used in consumer products can be very small and vary from approximately 90 μm in beverage cans down to a few microns when used as

a ply in packaging materials. Thin aluminum sheets or foils can also be used in electrical capacitors and as substrate carriers in solar cells.

Fine-grained materials – with grain sizes down to the nano-scale – are today frequently produced by exposing the material to severe plastic deformations. This can be achieved through any of a number of different processes such as equal channel angular pressing or extrusion (ECAP, ECAE), multi-directional forging (MDF), accumulated roll bonding (ARB), high-pressure torsion (HPT), twist extrusion (TE) and asymmetric rolling (ASR). A thorough study on ECAP is given in [6]. Asymmetric rolling of aluminum is discussed in [7] and ECAP processing of aluminum is studied in [8].

Asymmetric rolling was considered already in 1947 in [9]. Most experimental studies on asymmetric rolling have, however, been conducted from the mid 1960's and onward, mainly focusing on process parameters such as the angular velocities of the rolls, sheet thickness reduction rates and rolling friction or lubrication.

Several studies on the resulting curvature of asymmetrically rolled sheets have been presented. In the early work of [10], the resulting curvature after asymmetric rolling of lead strips is considered. Numerical simulations on the curvature of a C15 steel sheet after asymmetric cold rolling are discussed in [11].

Experimental determination of the roll pressure during rolling of different metals is done in [12] and in [13], experimental studies are performed on cold rolling with a roll speed mismatch, focusing on rolling loads.

The macroscopic results of asymmetric hot and cold rolling are studied in [14], both experimentally and analytically and in the latter case considering the sheet to be made of a rigid-plastic material.

Numerical simulations of rolling, by means of elasto-plastic FE analysis, are compared to experimental results in [15, 16] with focus on friction and contact stresses between sheet and rollers. The influence of temperature in 3D-simulations of rolling is considered in [17], using different thickness reductions per rolling pass. 3D-simulations of a rolling process are performed in [18], looking at rolling forces and contact stresses. Numerical simulation of rolling, focusing on ductile damage, is performed in [19].

Combined experimental analysis and simulation of the deformation and shear strain distribution in the sheet during asymmetric rolling is discussed in [20].

Studies on the texture evolution during asymmetric rolling of both pure aluminum and commercial purity grades are abundant in the published literature. Experimental studies of the texture evolution are presented in [7, 21, 22]. Numerical simulations of texture development during asymmetric rolling of aluminum are the topic in [23, 24]. These studies show that a pronounced rolling texture is developed in the material during rolling. This texture can, however, to a large extent be removed by subsequent annealing to achieve equiaxed grains in the final product.

Experimental investigations of the grain refinement in aluminum during asymmetric

rolling have been the subject of several publications. The possibilities to obtain refined grain structures from asymmetric rolling and accumulative roll bonding, respectively, are compared in [25]. Grain refinement in asymmetrically rolled aluminum is also determined experimentally in [26]. The mechanical properties of aluminum after asymmetric rolling are experimentally determined in [7]. Fine grained microstructures in an AA5754 aluminum alloy after asymmetric rolling and subsequent annealing are discussed in [27]. In [28], shear deformation texture and grain refinement after asymmetric rolling of aluminum are studied.

Grain refinement due to recrystallization during hot rolling is considered in [29] regarding steel sheets and numerical simulations of hot rolling of an AA5083 aluminum alloy are performed in [30]. Recrystallization is not a part of the hot rolling simulation, but is applied through empirically established relations in a post-processing step.

Modeling and simulation of the grain refinement due to dynamic recrystallization during cold rolling are less investigated. One account is found in [31], where the dislocation density-based model in [32] is employed in simulations of symmetric cold rolling of commercial purity AA1200 aluminum and titanium. To obtain a measure of grain refinement, the dislocation cell size was identified as the grain size in [31].

The present work concerns numerical simulations where advantage is taken of a constitutive model previously presented in [8]. The model is further developed in the present work and model parameters are calibrated to a different set of experimental data than was considered previously. The material parameters entering the model are set to comply with the properties of AA1050 aluminum. The focus of the present work lies on the influence of different process parameters on the dynamic recrystallization taking place during cold rolling. To the author's knowledge, no such study of dynamic recrystallization in AA1050 aluminum during symmetric/asymmetric cold rolling has been previously published.

The finite strain elasto-viscoplastic model employed in the present study takes the microstructure evolution into account in terms of evolving dislocation density and grain size. These quantities are allowed to influence macroscopic material properties such as flow stress and deformation-rate dependence. This is in contrast to the common approach in numerical simulations of metal forming where the grain size is assumed to be a constant parameter, if considered at all.

In addition to the recrystallized grain size, variations in plastic slip deformation in the rolled sheet due to different processing condition – on the microlevel manifested by the dislocation density and on the macrolevel by an effective plastic strain – are considered in the present work. This is vital in relation to recrystallization, but apart from the numerical simulations in [16, 31], this aspect has been given little attention in the published literature on simulations of cold rolling.

This paper is divided into sections, where section 2 gives a description of the material model and the calibration of the model against experimental data. Section 3 discusses the numerical implementation of the constitutive model. The resulting parameter values

related to AA1050 aluminum are presented. Section 4 describes numerical simulations of cold rolling of AA1050 aluminum sheets. Different process setups are studied in terms of the thickness reduction in each pass, different asymmetry ratios and different conditions of rolling friction. Results from the simulations are presented and discussed. Some concluding remarks close the paper in section 5.

2 Constitutive model

The framework for the finite strain elasto-viscoplastic model employed here was established previously in [8]. The model is for completeness briefly recapitulated below and modifications of the previous model are introduced.

Considering continuous dynamic recrystallization, the initial average grain size D_0 is in the model allowed to be gradually reduced as a function of the macroscopic effective viscoplastic strain $\varepsilon_{\text{eff}}^{\text{vp}}$. In [8], a steady-state saturation grain size D_{f} was defined. This saturation grain size was reached after a certain amount of macroscopic plastic deformation. In the present model, however, this saturation value is removed and instead the grain size is allowed to be further reduced, although slowly, also at large plastic strains. This is motivated by experimental evidence, given in e.g. [33], and is an essential feature of the present work where grain sizes down to the sub-micron level are considered. The present formulation of the grain size evolution has the format

$$D = D_0 - \left[D_0 - z_1 \exp\left(-z_2 \varepsilon_{\text{eff}}^{\text{vp}}\right)\right]\left[1 - \exp\left(-z_3 \left\langle \varepsilon_{\text{eff}}^{\text{vp}} - \varepsilon_{\text{c}}^{\text{vp}} \right\rangle^{z_4}\right)\right] \tag{1}$$

where z_i are parameters controlling the how fast the recrystallization proceeds with increasing plastic deformation. The McCauley brackets $\langle \cdot \rangle$ imply that recrystallization will be delayed until $\varepsilon_{\text{eff}}^{\text{vp}} > \varepsilon_{\text{c}}^{\text{vp}}$. Note that whereas the effective plastic strain measure entering eq. (1) was taken as a parameter dependent on the deformation mode in the previous model in [8], such deformation mode dependence is not present in the current formulation.

The critical threshold strain $\varepsilon_{\text{c}}^{\text{vp}}$ in eq. (1) is a measure of the incubation period required for subgrains to appear and gain enough misorientation to form new grains. Following [8], $\varepsilon_{\text{c}}^{\text{vp}} = 0.1$ is taken as a typical value for commercial-purity aluminum. Further, by setting $z_i = [1.1 \times 10^{-6}, 0.043, 3.7, 2]$, the grain size evolution in Fig. 1 is obtained where eq. (1) is plotted along with experimental data from [33–35]. Note that for the AA1050 aluminum presently under consideration, the experimental data in [33] is used and hence $D_0 = 29$ μm is chosen.

Since the experimental data in Fig. 1 was obtained by ECAP-processing, the data points are sparsely distributed. The grain size reduction, as described by eq. (1), therefore has an assumed form based on the available data. This assumed form, however, captures the initially very rapid reduction of grain size which, at a deformation of $\varepsilon_{\text{eff}}^{\text{vp}} \approx 1$, changes into a much slower grain size reduction rate.

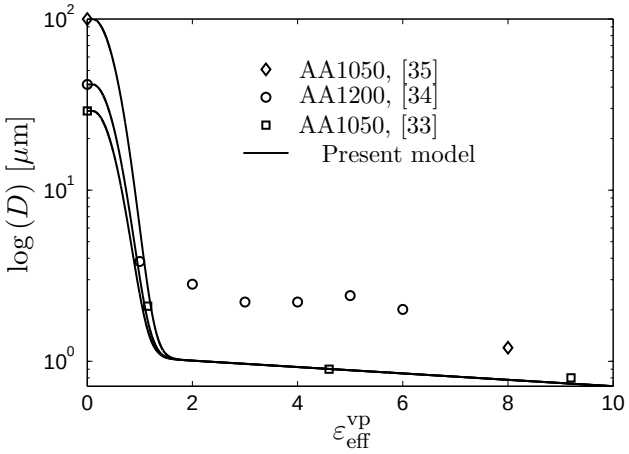

Figure 1: Grain size as function of plastic deformation for various aluminum grades. The present model (solid lines) is calibrated against experimental data (symbols). Note the logarithmic scale on the vertical axis. In the present simulations, the data from [33] with an initial grain size of 29 μm has been used, shown by square symbols (□).

Following [36, 37], the evolution of the dislocation density ρ_{d} in the material is taken to progress according to

$$\dot{\rho}_{\text{d}} = \left(\bar{d}_1\sqrt{\rho_{\text{d}}} - \bar{d}_2\rho_{\text{d}}\right)\dot{\varepsilon}_{\text{eff}}^{\text{vp}} \tag{2}$$

where $\bar{d}_1$ and $\bar{d}_2$ are parameters controlling the generation and annihilation of dislocations, respectively. If the evolving grain size is also considered, eq. (2) has to be modified to take into account the mean-free path for dislocation movement. The mean-free path is influenced by both the spacing between dislocations and by the grain boundaries which pose obstacles to dislocation motion. Such considerations add a term proportional to $1/D + \sqrt{\rho_{\text{d}}}$ to eq. (2). The $\sqrt{\rho_{\text{d}}}$-proportionality is taken into account by $\bar{d}_1$ which leaves the $1/D$ component to be included, resulting in a modified form of eq. (2), appearing as

$$\frac{\dot{\rho}_{\text{d}}}{\rho_{\text{d}}^0} = \left(d_1\sqrt{\frac{\rho_{\text{d}}}{\rho_{\text{d}}^0}} - d_2\frac{\rho_{\text{d}}}{\rho_{\text{d}}^0} + d_3\frac{D_0}{D}\right)\dot{\varepsilon}_{\text{eff}}^{\text{vp}} \tag{3}$$

where the dislocation density has been normalized by its initial value ρ_{d}^0 and the grain size by D_0. Again, d_1, d_2 and d_3 are constitutive parameters.

The microstructure parameters D and ρ_{d} are in the model allowed to influence the macroscopic yield stress σ_{y} of the material. The influence of grain size on the macroscopic yield stress can be considered through the Hall-Petch relation which has been experimentally confirmed to be valid for aluminum over a wide range of grain sizes in [38–41]. This indicates the proportionality $\sigma_{\text{y}} \propto D^{-1/2}$. In addition, the dislocation mobility and hence also the progression of plastic flow will become increasingly difficult as the dislocation density increases. On a macroscopic level this is manifested as a deformation hardening of the

material. This yields the proportionality $\sigma_{\mathrm{y}} \propto \sqrt{\rho_{\mathrm{d}}}$ as discussed in [36, 37, 42, 43]. Taking these flow stress components together, the macroscopic flow stress can be written as

$$\sigma_{\mathrm{y}} = \sigma_{\mathrm{y0}} + H\left(\sqrt{\frac{\rho_{\mathrm{d}}}{\rho_{\mathrm{d}}^{0}}} - 1\right) + k_{\mathrm{D}}\left(\sqrt{\frac{D_0}{D}} - 1\right) \tag{4}$$

where H is a hardening modulus corresponding to a generalized Taylor factor, k_{D} is a stress intensity factor and σ_{y0} is the Peierls stress, allowing the initial yield stress of the undeformed material to be written as $\sigma_{\mathrm{y0}} = \sigma_{\mathrm{y}}\left(\rho_{\mathrm{d}}^{0}, D_0\right)$.

Considering the experimental data on ECAE-processed AA1050 aluminum presented in [33], the parameters in the expression for the yield stress, eq. (4), and in the dislocation density evolution equation, eq. (3), can be fitted. The resulting calibration is shown in Fig. 2, where the parameter set $\sigma_{\mathrm{y0}} = 50$ MPa, $k_{\mathrm{D}} = 4.3$ MPa and $H = 0.96$ MPa was used. In addition, the initial dislocation density was set to $\rho_{\mathrm{d}}^{0} = 1 \times 10^{9}$ m^{-2}, in line with [44]. To obtain the calibration in Fig. 2, initial values in the case of no ECAE-processing were obtained as $(D, \rho_{\mathrm{d}}/\rho_{\mathrm{d}}^{0}) = (29\ \mu\mathrm{m}, 1)$, for one ECAE pass $(D, \rho_{\mathrm{d}}/\rho_{\mathrm{d}}^{0}) = (2.4\ \mu\mathrm{m}, 3.8 \times 10^{3})$ and for eight ECAE passes $(D, \rho_{\mathrm{d}}/\rho_{\mathrm{d}}^{0}) = (0.8\ \mu\mathrm{m}, 4.4 \times 10^{3})$. The calibration procedure results in the parameter values $d_1 = 279.5$, $d_2 = 7.7$ and $d_3 = 437.5$.

The grain size will not only influence the macroscopic yield stress of the material, but also the macroscopic strain-rate dependence. Coarse-grained materials tend to be relatively rate independent while materials with a finer grain structure are more sensitive to the deformation rate. The grain size influence on the strain-rate dependence of aluminum has been confirmed experimentally in [45–48]. The viscoplastic formulation of the present

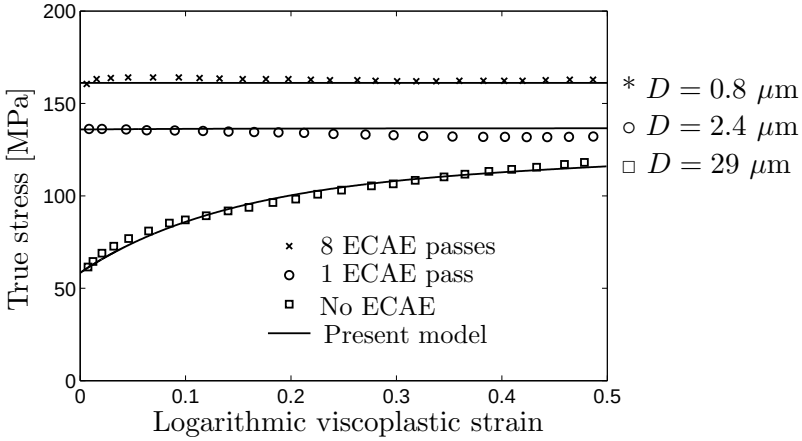

Figure 2: The results from the present model (solid lines) are calibrated against experimental data (symbols) for axisymmetric compression tests on AA1050 aluminum after different number of ECAE passes. The experimental data is taken from [33].

model is achieved by defining the effective viscoplastic strain rate as

$$\dot{\varepsilon}_{\text{eff}}^{\text{vp}} = \frac{1}{\eta} h\left(\sigma_{\text{eff}}, \rho_{\text{d}}, D\right) \tag{5}$$

where η is a viscosity parameter and h an over-stress function. The effective Von Mises stress is defined as $\sigma_{\text{eff}} = \sqrt{3J_2}$ where $J_2 = \frac{1}{2}\text{tr}\left(\boldsymbol{\tau}^{\text{dev}}\boldsymbol{\tau}^{\text{dev}}\right)$ is the second invariant of the deviatoric stress tensor. The deviatoric part of the Kirchhoff stress tensor is denoted by $\boldsymbol{\tau}^{\text{dev}}$ and the trace of a tensorial quantity by $\text{tr}(\cdot)$. The over-stress function h appearing in eq. (5) is assumed to have the format

$$h = \left\langle \frac{\sigma_{\text{eff}} - \sigma_{\text{y}}}{\sigma_{\text{y0}} + k_{\text{D}}\left(\sqrt{\frac{D_0}{D}} - 1\right)} \right\rangle^{m(D)} \tag{6}$$

The rate dependence of the model is by this formulation controlled by the parameter $m(D)$ which is assumed to depend on the grain size according to

$$m(D) = 1 + m_1 \exp\left[m_2\left(1 - \frac{D}{D_0}\right)\right] \tag{7}$$

where m_1 and m_2 are model parameters. Combining eqs. (5) and (6), a dynamic yield function can be defined as

$$f^{\text{d}} = \sigma_{\text{eff}} - \sigma_{\text{y}}^{\text{d}}\left(D, \dot{\varepsilon}_{\text{eff}}^{\text{vp}}\right) - H\left(\sqrt{\frac{\rho_{\text{d}}}{\rho_{\text{d}}^0}} - 1\right) \tag{8}$$

where the rate dependence of the model becomes apparent if considering the dynamic yield stress $\sigma_{\text{y}}^{\text{d}}$ in eq. (8) which appears as

$$\sigma_{\text{y}}^{\text{d}}\left(D, \dot{\varepsilon}_{\text{eff}}^{\text{vp}}\right) = \left[\sigma_{\text{y0}} + k_{\text{D}}\left(\sqrt{\frac{D_0}{D}} - 1\right)\right]\left[1 + \left(\eta\dot{\varepsilon}_{\text{eff}}^{\text{vp}}\right)^{1/m(D)}\right] \tag{9}$$

Fig. 3 shows the rate dependence of the model calibrated against the experimental data in [47]. This is calibration is obtained by keeping the viscosity parameter constant at $\eta = 4 \times 10^{-4}$ while setting $m_1 = 0.0014$ and $m_2 = 8.5$. Note that the parameter k_{D} is already calibrated. The strain rate sensitivity of the model will by the formulation in eq. (7) weaken as the grain size is increased, i.e. as m approaches unity.

A finite strain viscoplastic model is established based on the micromechanical quantities just introduced. The finite strain kinematics are based on a multiplicative split of the deformation gradient $\boldsymbol{F}$ into one component $\boldsymbol{F}^{\text{e}}$ related to the elastic deformation and one component $\boldsymbol{F}^{\text{vp}}$ related to the viscoplastic deformation, giving $\boldsymbol{F} = \boldsymbol{F}^{\text{e}}\boldsymbol{F}^{\text{vp}}$. The elastic behavior of the model is assumed to be governed by a strain energy function given by

$$W = K\frac{1}{2}\ln\left(J^{\text{e}}\right)^2 + 2GJ_2^{\text{e}} \tag{10}$$

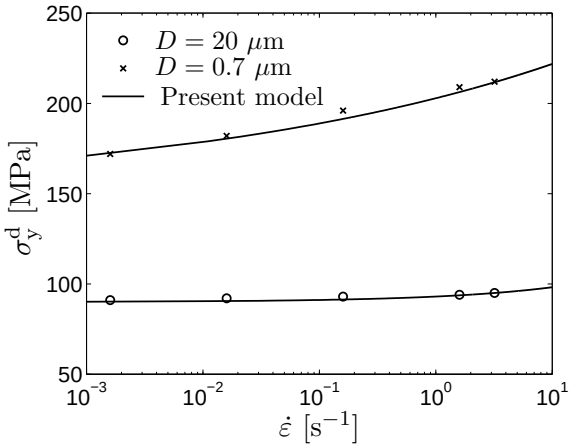

Figure 3: Variation of the macroscopic dynamic yield stress with strain rate for different grain sizes D. The present model (solid lines) is calibrated against experimental results in [47] on 99.5 % purity aluminum. Note the logarithmic scale on the horizontal axis

where $J^{\mathrm{e}} = \det(\boldsymbol{F}^{\mathrm{e}})$ while K and G correspond to the bulk and shear modulus, respectively, in the limit of small strains. Considering typical values for aluminum, these parameters are taken as $K = 56$ GPa and $G = 27$ GPa. The elastic left Cauchy-Green tensor is defined as $\boldsymbol{b}^{\mathrm{e}} = \boldsymbol{F}^{\mathrm{e}}\boldsymbol{F}^{\mathrm{eT}}$ and the left stretch tensor by $\boldsymbol{V}^{\mathrm{e}} = \sqrt{\boldsymbol{b}^{\mathrm{e}}}$. In addition, the quantity $J_2^{\mathrm{e}} = \frac{1}{2}(\ln \boldsymbol{V}^{\mathrm{e}})^{\mathrm{dev}} : (\ln \boldsymbol{V}^{\mathrm{e}})^{\mathrm{dev}}$ was introduced in eq. (10). Here, $(\cdot) : (\cdot)$ denotes a tensorial contraction over two indices. From the strain energy function in eq. (10), the Kirchhoff stress tensor is obtained as

$$\boldsymbol{\tau} = 2\boldsymbol{b}^{\mathrm{e}}\frac{\partial W}{\partial \boldsymbol{b}^{\mathrm{e}}} = K\ln(J^{\mathrm{e}})\,\mathbf{1} + 2G\ln(\boldsymbol{V}^{\mathrm{e}}) \tag{11}$$

where $\mathbf{1}$ is the second order identity tensor.

Considering the inelastic behavior of the model, the viscoplastic rate of deformation tensor is defined as $\boldsymbol{d}^{\mathrm{vp}} = \mathrm{sym}\left(\dot{\boldsymbol{F}}^{\mathrm{vp}}\boldsymbol{F}^{\mathrm{vp}-1}\right)$ where $\mathrm{sym}(\cdot)$ indicates the symmetric part of a tensorial quantity. Adopting J_2-plasticity, the evolution of $\boldsymbol{d}^{\mathrm{vp}}$ is given by

$$\boldsymbol{d}^{\mathrm{vp}} = \dot{\varepsilon}_{\mathrm{eff}}^{\mathrm{vp}}\frac{3}{2}\frac{\boldsymbol{\tau}_{\mathrm{r}}^{\mathrm{dev}}}{\sigma_{\mathrm{eff}}} \tag{12}$$

where $\boldsymbol{\tau}_{\mathrm{r}}^{\mathrm{dev}} = \boldsymbol{R}^{\mathrm{eT}}\boldsymbol{\tau}^{\mathrm{dev}}\boldsymbol{R}^{\mathrm{e}}$ is the elastically rotated deviatoric Kirchhoff stress tensor.

3 Numerical implementation

The constitutive model is implemented as a user subroutine (VUMAT) in Abaqus Explicit, using a fully implicit backward Euler integration procedure for the constitutive equations.

Seeking computational efficiency, the approach put forward in [49] is followed. To this end, two consecutive load steps are denoted by n and $n+1$, respectively, allowing an exponential update scheme to be defined as

$$\boldsymbol{F}^{\mathrm{e}}_{n+1} = \boldsymbol{A}^{-1}\boldsymbol{F}^{\mathrm{e,trial}} \qquad \text{where} \qquad \boldsymbol{A} = \exp\left[\Delta\varepsilon^{\mathrm{vp}}_{\mathrm{eff}}\left(\frac{3}{2}\frac{\boldsymbol{\tau}^{\mathrm{dev}}}{\sigma_{\mathrm{eff}}}\right)_{n+1}\right] \tag{13}$$

This scheme is used to update the reversible part of the deformation gradient from a trial state – denoted by a superscript trial – to the current state. The elastic trial state is obtained by freezing the plastic flow, giving $\boldsymbol{F}^{\mathrm{e,trial}}_{n+1} = \boldsymbol{F}_{n+1}\boldsymbol{F}^{\mathrm{vp}-1}_{n}$. Using eq. (13), the elastic left Cauchy-Green tensor can be written as

$$\boldsymbol{b}^{\mathrm{e}}_{n+1} = \boldsymbol{F}^{\mathrm{e}}_{n+1}\left(\boldsymbol{F}^{\mathrm{e}}_{n+1}\right)^{\mathrm{T}} = \boldsymbol{A}^{-1}\boldsymbol{b}^{\mathrm{e,trial}}\boldsymbol{A}^{-\mathrm{T}} \tag{14}$$

For a purely elastic material response the update can be achieved by setting $(\cdot)_{n+1} = (\cdot)^{\mathrm{trial}}$. In the case of inelastic loading, an exponential update of $\boldsymbol{F}^{\mathrm{vp}}$ can be performed together with a backward Euler update of $\varepsilon^{\mathrm{vp}}_{\mathrm{eff}}$. Combining eqs. (5) and (14), a system of nonlinear equations can be formulated as

$$\begin{aligned} &\boldsymbol{\mathcal{R}}_{\boldsymbol{b}^{\mathrm{e}}} = \boldsymbol{b}^{\mathrm{e}}_{n+1} - \boldsymbol{A}^{-1}\boldsymbol{b}^{\mathrm{e,trial}}\boldsymbol{A}^{-\mathrm{T}} = \boldsymbol{0} \\ &\mathcal{R}_{\Delta\varepsilon^{\mathrm{vp}}_{\mathrm{eff}}} = \eta\frac{\Delta\varepsilon^{\mathrm{vp}}_{\mathrm{eff}}}{\Delta t} - h = 0 \end{aligned} \tag{15}$$

These equations can be addressed using the eigenvalue decomposition theorem. Taking the logarithm of (15a) yields

$$\ln\left(\boldsymbol{V}^{\mathrm{e}}\right)^{\mathrm{dev}} = \ln\left(\boldsymbol{V}^{\mathrm{e,trial}}\right)^{\mathrm{dev}} - \Delta\varepsilon^{\mathrm{vp}}_{\mathrm{eff}}\left(\frac{3}{2}\frac{\boldsymbol{\tau}^{\mathrm{dev}}}{\sigma_{\mathrm{eff}}}\right) \tag{16}$$

Using eqs. (11)-(12), it is now found that

$$\boldsymbol{\tau}^{\mathrm{dev}} = \boldsymbol{\tau}^{\mathrm{dev,trial}} - 3G\Delta\varepsilon^{\mathrm{vp}}_{\mathrm{eff}}\frac{\boldsymbol{\tau}^{dev}}{\sigma_{\mathrm{eff}}} \qquad \text{where} \qquad \boldsymbol{\tau}^{\mathrm{dev,trial}} = 2G\ln\left(\boldsymbol{V}^{\mathrm{e,trial}}\right)^{\mathrm{dev}} \tag{17}$$

which can be further reduced to the format

$$\sigma_{\mathrm{eff}} = \sigma^{\mathrm{trial}}_{\mathrm{eff}} - 3G\Delta\lambda \qquad \text{where} \qquad \sigma^{\mathrm{trial}}_{\mathrm{eff}} = \left(\frac{3}{2}\boldsymbol{\tau}^{\mathrm{dev,trial}} : \boldsymbol{\tau}^{\mathrm{dev,trial}}\right)^{1/2} \tag{18}$$

The equations in (15) can now be reduced to the single scalar equation

$$\begin{aligned} &\mathcal{R}\left(\Delta\varepsilon^{\mathrm{vp}}_{\mathrm{eff}}\right) = \eta\frac{\Delta\varepsilon^{\mathrm{vp}}_{\mathrm{eff}}}{\Delta t} - h = 0 \qquad \text{where} \\ &h = \left\langle\frac{\sigma^{\mathrm{trial}}_{\mathrm{eff}} - 3G\Delta\varepsilon^{\mathrm{vp}}_{\mathrm{eff}} - \sigma_{\mathrm{y}}\left(\varepsilon^{vp}_{\mathrm{eff},n} + \Delta\varepsilon^{\mathrm{vp}}_{\mathrm{eff}}, \theta\right)}{\sigma_{\mathrm{y}}\left(0,\theta\right)}\right\rangle^{n} \end{aligned} \tag{19}$$

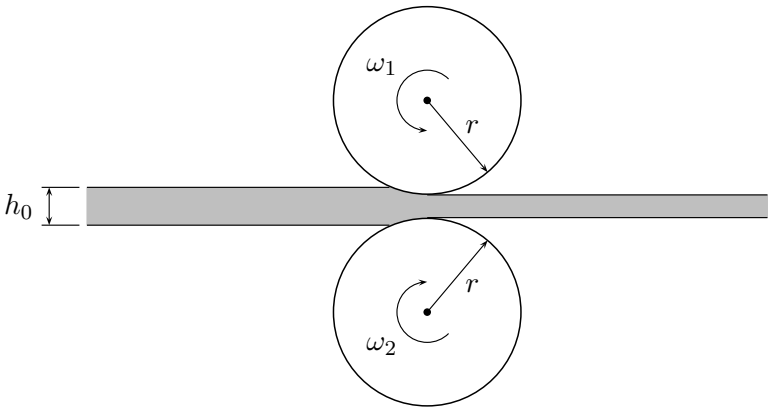

Figure 4: Schematic illustration of the rolling process of a sheet with initial thickness h_0. Keeping the radii r equal for both rollers, symmetric rolling is achieved when the angular velocities fulfill $\omega_1 = \omega_2$ and asymmetric rolling is obtained for $\omega_1 \neq \omega_2$.

With the evolution law for the dislocation density in eq. (3), the local stress-updating algorithm now only involves two scalar equations which can be treated numerically efficient.

Numerical implementation of constitutive models, using the above approach, is also discussed in [8, 50].

4 Numerical simulations of cold rolling

This section considers numerical 2D-simulations of cold rolling. The process setup is illustrated in Fig. 4, where an aluminum sheet with initial thickness $h_0 = 1$ mm is allowed to pass between two rolls having the same radius $r = 50$ mm.

Asymmetry can be induced into the rolling process by prescribing different angular velocities of the upper and lower rolls, by having rolls of different radii rotating at the same angular velocity or by keeping velocities and roll dimensions equal but varying the friction conditions on opposite sides of the sheet. These approaches are discussed in [10, 11, 51].

In the present case, the angular velocity ω_2 of the lower roll is kept constant while the angular velocity ω_1 of the upper roll is gradually increased, i.e. $\omega_1 \geq \omega_2$. The angular velocity of the lower roll is held constant at $\omega_2 = 3$ rad/s, a value also considered in [18]. Due to the process setup, plane strain conditions are assumed in line with [12, 15, 23].

The frictional conditions at the interfaces between the rollers and the sheet are modeled by Coulomb friction, defined by a constant friction coefficient μ. Identical frictional contact conditions are assumed between the sheet and each of the rolls. The influence of friction on the rolling process is discussed further below.

The sheet is discretized using a regular grid of 10,000 quadrilateral bi-linear elements of type CPE4R, taking advantage of reduced integration for computational efficiency. The sheet thickness is resolved by 10 elements. The sheet material is taken to be AA1050

Table 1: Material parameters entering the present model.

Parameter	Value	Description
d_1	279.5	Parameter controlling the creation of dislocations
d_2	7.7	Parameter controlling the annihilation of dislocations
d_3	437.5	Parameter controlling the influence of grain size on the dislocation density
z_1	1.1×10^{-6}	Coefficient in the grain size evolution law
z_1	0.043	Coefficient in the grain size evolution law
z_2	3.7	Coefficient in the grain size evolution law
z_3	2	Exponent in the grain size evolution law
k_{D}	4.3 MPa	Stress intensity factor in the Hall-Petch relation
D_0	29 μm	Initial average grain size
ρ_{d}^0	1×10^9 m^{-2}	Initial dislocations density
$\varepsilon_{\mathrm{c}}^{\mathrm{vp}}$	0.1	Critical viscoplastic strain at which recrystallization is initiated
η	4×10^{-4} s	Viscosity parameter in the over-stress formulation
m_1	0.0014	Parameter controlling the grain size dependent rate sensitivity
m_2	8.5	Parameter controlling the grain size dependent rate sensitivity
σ_{y0}	50 MPa	Initial yield stress
K	56 GPa	Bulk modulus
G	27 GPa	Shear modulus
H	0.96 MPa	Isotropic hardening modulus

aluminum and the material parameters summarized in Table 1. With these values of D_0 and ρ_{d}^0, the undeformed conditions thus represent an annealed and relatively coarse-grained material.

In the subsequent simulations, three rolling processes are studied with thickness reductions of 20 %, 40 % and 60 % in each pass, respectively. Two rolling passes are simulated for each situation. Each simulation run is begun by vertically displacing the rollers – which are just contacting the top and bottom edges of the sheet at one end – through a prescribed distance. Their positions are then fixated while given appropriate angular velocities. The frictional contact between the sheet and the rollers drags the sheet between the rollers. After the first pass, the rotation of the rollers is stopped and they are again displaced vertically. The rotation of the rollers is then reversed and the sheet is rolled once again, now in the reverse direction.

Section 4.1 studies the influence of the magnitude of Coulomb friction between the sheet and the rollers and section 4.2 is concerned with the effects of varying degrees of rolling asymmetry. The combined effects of rolling asymmetry and increased rolling friction are discussed in section 4.3.

4.1 Influence of friction

The transport of sheet material between the rollers and the level of plastic deformation of the sheet is strongly influenced by the magnitude of the friction coefficient μ. To illustrate

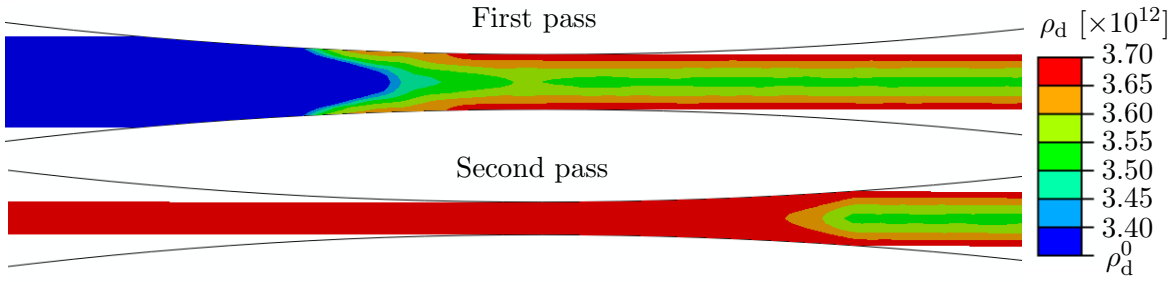

Figure 5: Distribution of dislocation density obtained from a symmetric rolling operation with 40 % thickness reduction per pass and a rolling friction of $\mu = 0.25$. The top figure shows the results after the first pass and the bottom figure after the second pass.

these effects, a series of simulations of symmetric rolling were performed with $\omega_1 = \omega_2$, cf. Fig. 4.

Three levels of Coulomb friction were applied by setting $\mu = 0.15$, $\mu = 0.2$ and $\mu = 0.25$, respectively. The smallest value was chosen following the simulation parameters used in [15, 18, 19]. The larger values of μ were set to study the influence of increasing frictional contact between the sheet and the rollers.

To illustrate a typical simulation result, Fig. 5 illustrates the distribution of dislocation density obtained during symmetric rolling with a thickness reduction of 40 % per pass and with a rolling friction of $\mu = 0.25$. Fig. 5 shows the results after one (top) and two (bottom) passes, respectively. In the following, simulation results are instead presented as graphs of the through-thickness variation of variables for clarity and easier comparison of results.

Presented through-thickness variations of a variable is obtained from the mid section of the modeled sheet where the influence of the ends of the sheet is assumed negligible.

Fig. 6 shows the influence of the value of the friction coefficient μ on the through-thickness variation of effective plastic strain in the sheet at the three different thickness reduction ratios under consideration and after one and two rolling passes, respectively.

From Fig. 6 it can be noted that increasing the thickness reduction per pass has a significant impact on the amount of plastic deformation of the material. Looking at the through-thickness variation of effective plastic strain in Fig. 6, it is apparent that the plastic deformation is most pronounced near the top and bottom surfaces of the rolled sheet. This tendency is further emphasized as increasing values of the friction coefficient μ are considered and most significantly after the second rolling pass.

On the level of the microstructure, the measure of plastic deformation is the dislocation density ρ_d. The through-thickness variation of the dislocation density, normalized by the initial value ρ_d^0, is shown in Fig. 7. Consistent with the appearance of the effective

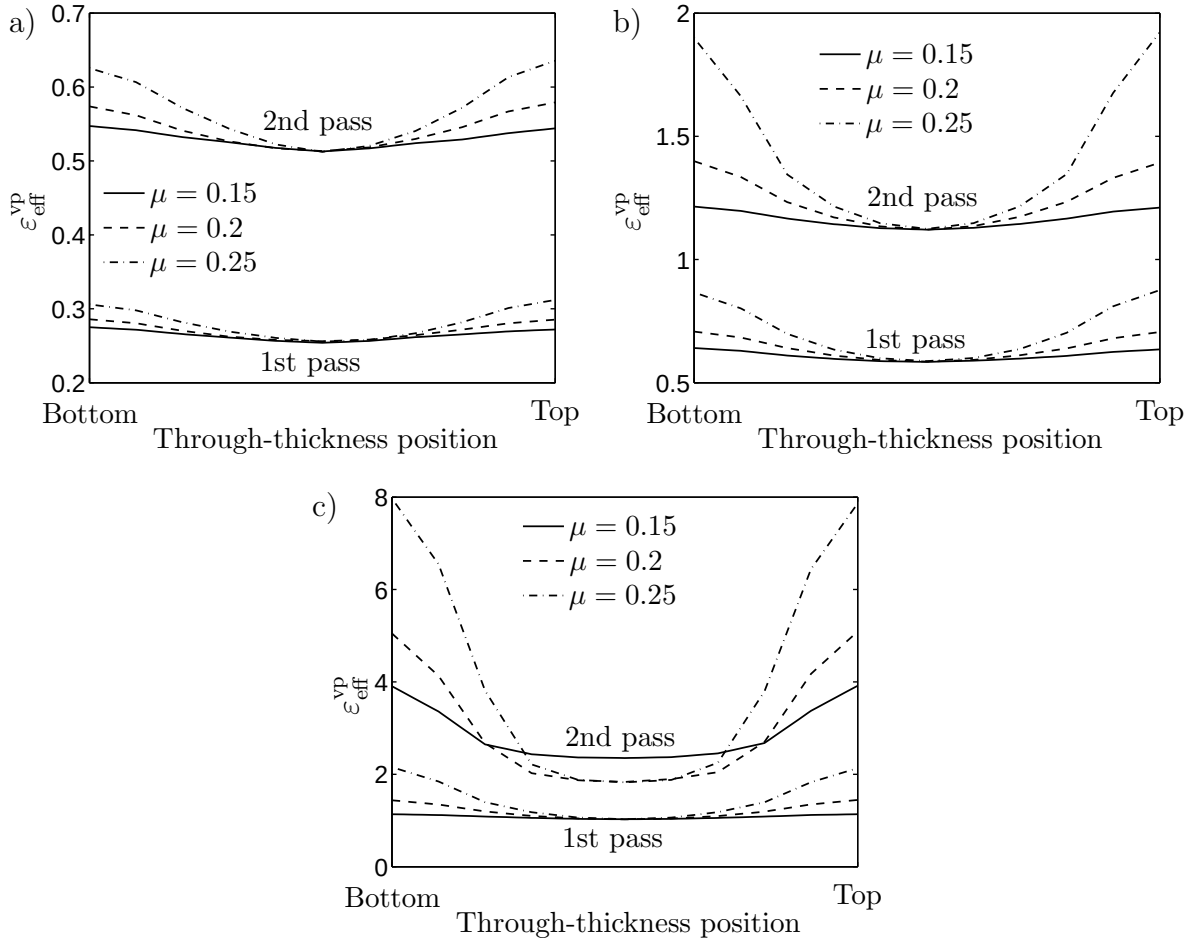

Figure 6: Influence of level of friction between sheet and rollers on the through-thickness variation of the effective plastic strain in the sheet after one and two rolling passes, respectively. Results are obtained at thickness reductions (per pass) of: (a) 20 %, (b) 40 % and (c) 60 %.

viscoplastic strain in Fig. 6, also the dislocation density attains its highest values in the vicinity of the top and bottom surfaces of the sheet. Considering the distribution of dislocation density at a thickness reduction of 60 % per pass in Fig. 7c, it can be noted that after two rolling passes, the dislocation density has saturated to a nearly constant value throughout the sheet thickness. Comparing with Fig. 6c, this saturation has taken place for values of the effective viscoplastic strain of $\varepsilon_{\text{eff}}^{\text{vp}} \geq 2$. This is again consistent with the macroscopic deformation hardening of the material, as illustrated in Fig. 2 for lower levels of plastic strain.

Recalling the format of eq. (1), the average grain size D evolves as a function of the effective viscoplastic strain $\varepsilon_{\text{eff}}^{\text{vp}}$. The through-thickness variation of the average grain size is shown in Fig. 8 and in line with the findings in Figs. 6 and 7, the grain refinement is

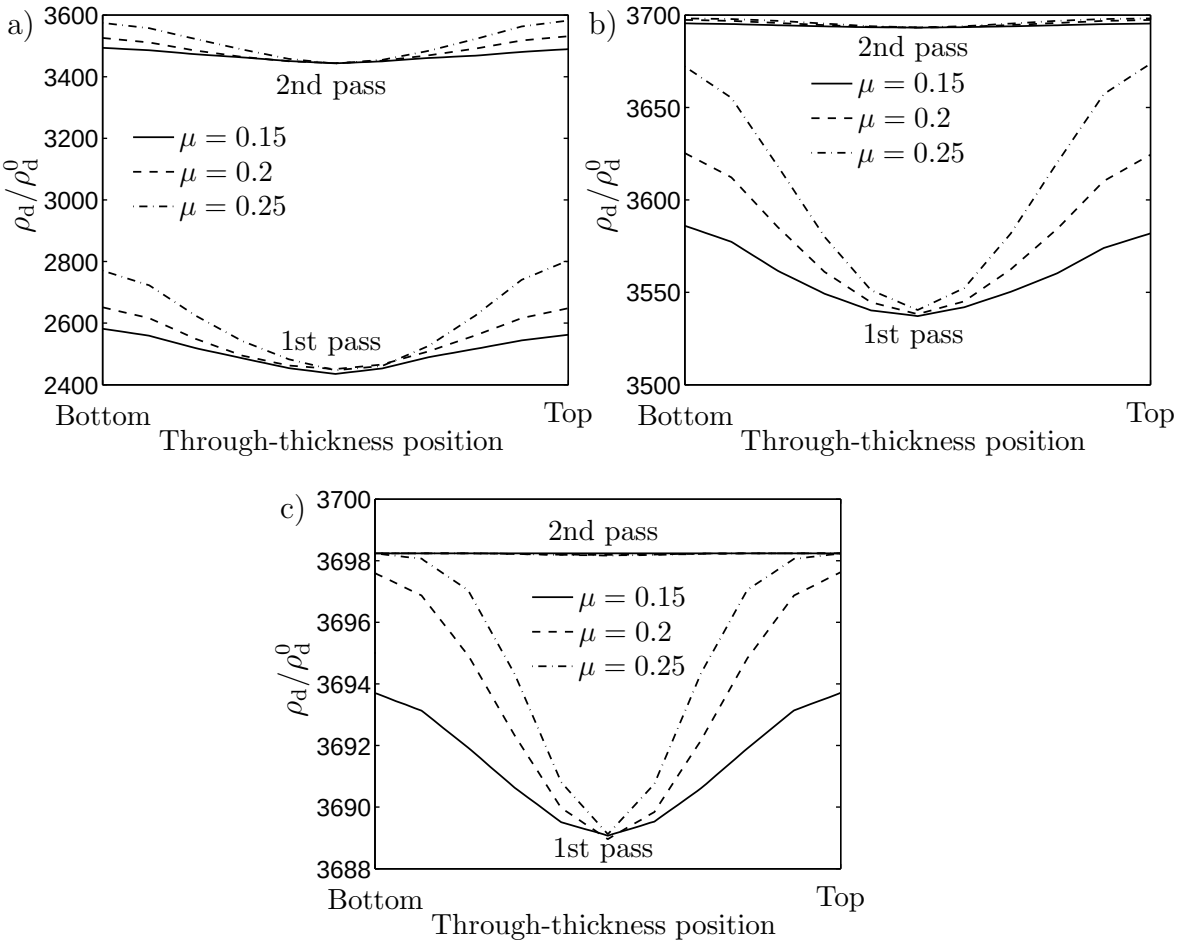

Figure 7: Influence of level of friction between sheet and rollers on the through-thickness variation of the normalized dislocation density in the sheet after one and two rolling passes, respectively. Results are obtained at thickness reductions (per pass) of: (a) 20 %, (b) 40 % and (c) 60 %.

most significant in the surface regions of the sheet which have been exposed to the most plastic deformation.

For all of the three thickness reduction ratios presently under consideration, grain refinement takes place throughout the entire thickness of the sheet. But whereas only minor grain size changes have taken place after one rolling pass at 20 % thickness reduction, cf. Fig. 8a, the effect is drastic at 60 % thickness reduction already after one rolling pass and at the lower friction of $\mu = 0.15$, cf. Fig. 8c. The grain refinement becomes even more pronounced as two rolling passes and higher values of the friction coefficient are considered. However, also at $\mu = 0.15$, sub-micron grain sizes are reached after two rolling passes at 60 % thickness reduction per pass, cf. Fig. 8c. Again, the grain refinement is most significant just below the top and bottom surfaces of the sheet.

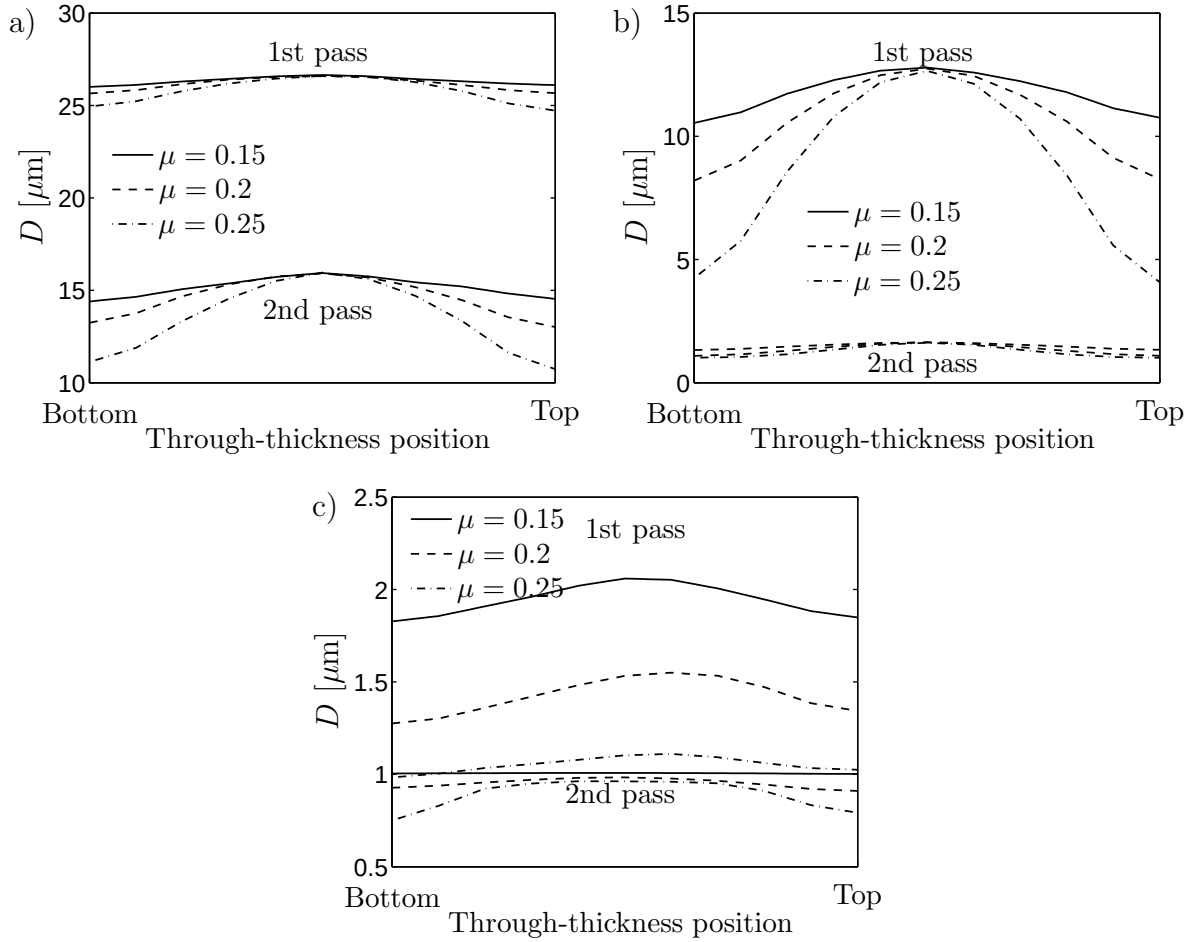

Figure 8: Influence of level of friction between sheet and rollers on the through-thickness variation of the average grain size in the sheet after one and two rolling passes, respectively. Results are obtained at thickness reductions (per pass) of: (a) 20 %, (b) 40 % and (c) 60 %.

The variation of rolling force with the level of friction is shown in Fig. 9. Symbols indicate the actual data points and the lines are just included to indicate the trends. The mean rolling forces during the first and second pass are shown by solid and dashed lines, respectively.

For all thickness reduction ratios, an increased friction results in increased rolling forces. This trend seems to be enhanced as greater thickness reduction ratios are considered. Accordingly, the slope of the lines at 60 % thickness reduction is greater than those found at 20 and 40 % reduction.

The magnitudes of the rolling forces become quite significant at high friction and high thickness reduction values. A slightly different rolling process setup – with 2 mm sheet thickness, 105 mm roller radii, and 10 % asymmetry in the angular velocities of the rollers – is considered in [14]. However, the force levels at $\mu = 0.15$, shown in Fig. 9, are of

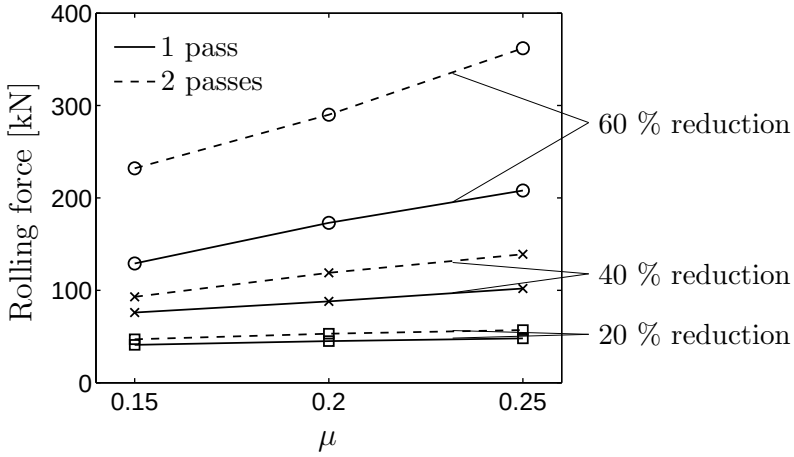

Figure 9: Influence of level of friction between sheet and rollers on mean rolling force during the first rolling pass (solid lines) and during the second rolling pass (dashed lines). Results are obtained at three different thickness reductions (per pass); 20 % (□), 40 % (×) and 60 % (○).

comparable magnitude to those found experimentally in [14] for A1050P aluminum.

4.2 Influence of rolling asymmetry

An asymmetric rolling process is desirable since it introduces additional shear deformation, and hence potentially also additional plastic deformation in the sheet material. Grain size reduction through dynamic recrystallization is driven by the plastic deformation and finer grain sizes can be expected as the level of asymmetry is increased.

Rolling asymmetry is introduced into the process by increasing the angular velocity ω_1 of the top roller relative to the angular velocity ω_2 of the bottom roller, cf. Fig. 4. The angular velocity of the bottom roller is kept constant at $\omega_2 = 3$ rad/s while the angular velocity ω_1 of the top roller is set to 4.5 and 6 rad/s, respectively. Choosing $\omega_1 = 3$ rad/s results in the symmetric rolling process considered previously in relation to variations in the frictional conditions.

Fig. 10 shows the through-thickness variation of the effective viscoplastic strain at the three thickness reduction ratios under consideration and at asymmetry ratios ω_1/ω_2 of 1.5 and 2. The results from the symmetric rolling simulations with $\omega_1/\omega_2 = 1$, cf. Fig. 6, are included in Fig. 10 for easier comparison. Note that the results in Figs. 10-12 are obtained using a rolling friction of $\mu = 0.15$. The influence of varying frictional conditions in combination with rolling asymmetry is studied in the next section.

It is apparent from Fig. 10 that the thickness reduction ratio has a more significant impact on the amount of plastic deformation than the asymmetry ratio. From Fig. 10, it

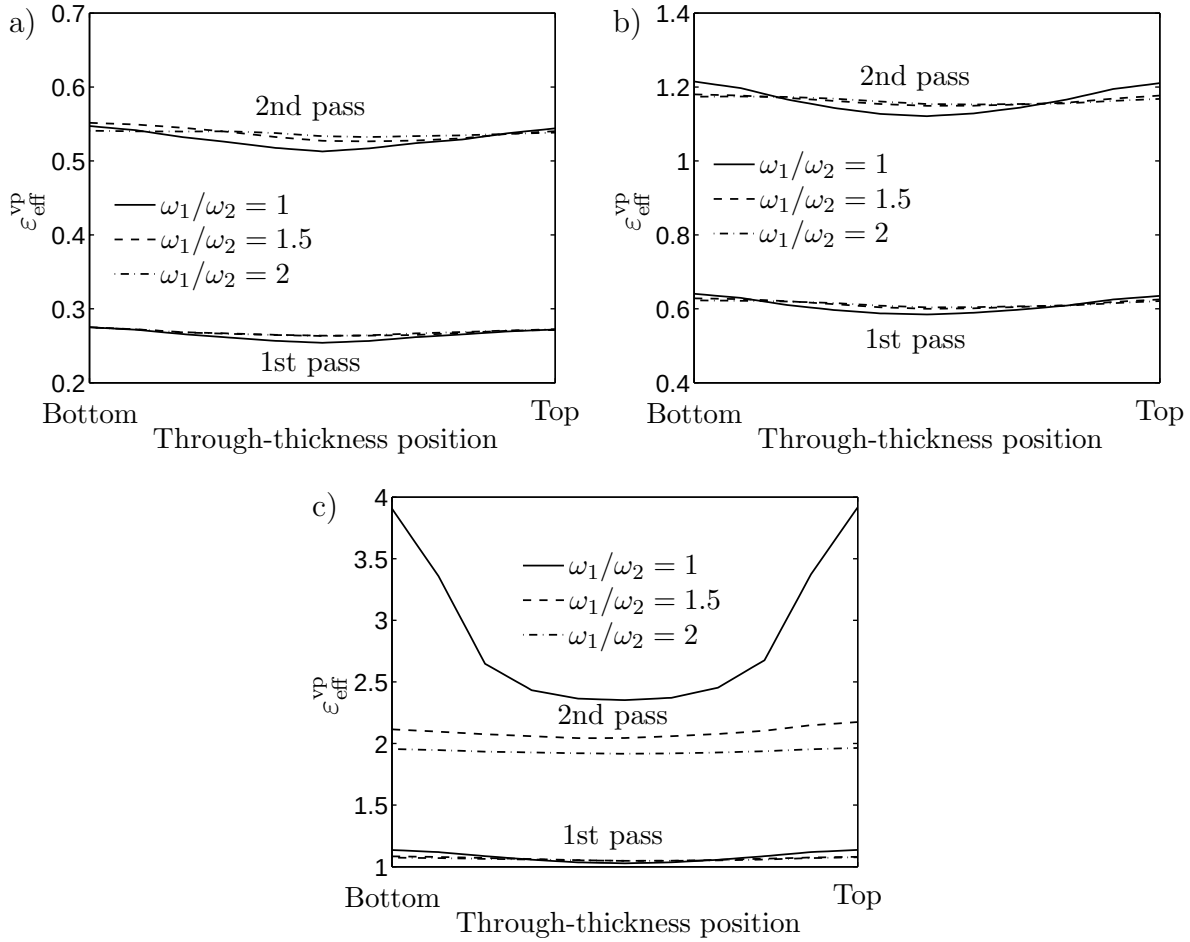

Figure 10: Influence of rolling asymmetry on the through-thickness variation of the effective plastic strain in the sheet after one and two rolling passes, respectively. Results are obtained at thickness reductions (per pass) of: (a) 20 %, (b) 40 % and (c) 60 %.

is also evident that the amount of plastic deformation obtained in the simulations is more impacted by adding a second rolling pass than by increasing the rolling asymmetry.

The results in Fig. 10 also illustrate how an increased asymmetry in the rolling process decreases the highest values of effective plastic strain at the surfaces of the sheet, making the through-thickness variation more even. This tendency is also observed experimentally during rolling of AA6111 aluminum in [21] and of AA5754 aluminum in [20].

Especially at the thickness reduction of 60 %, cf. Fig. 10c, the introduction of asymmetry lowers the high values of effective plastic strain encountered after two passes in the symmetric simulation (solid line). As discussed in [51], the presence of rolling asymmetry reduces the rolling pressure and alleviates the plastic deformation due to this deformation component. This was also observed in experiments in [21] where the formability of the sheet, in terms of the plastic strain ratio, was found to decrease with increased rolling

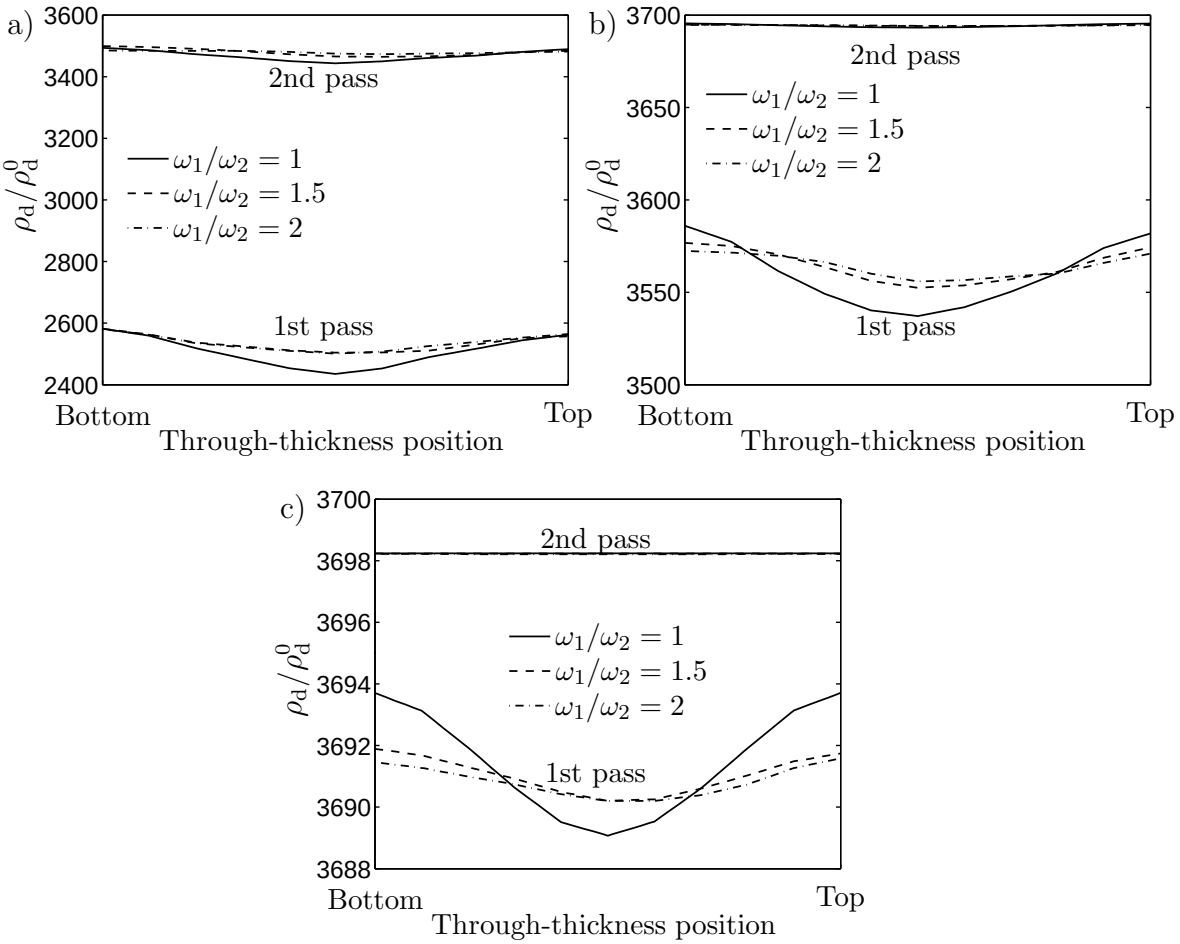

Figure 11: Influence of rolling asymmetry on the through-thickness variation of the normalized dislocation density in the sheet after one and two rolling passes, respectively. Results are obtained at thickness reductions (per pass) of: (a) 20 %, (b) 40 % and (c) 60 %.

asymmetry.

As another measure of plastic deformation, also the through-thickness distribution of normalized dislocation density, shown in Fig. 11, mirrors the trends in Fig. 10. Looking at Fig. 11, an increased thickness reduction per rolling pass has more influence on the dislocation density than the amount of asymmetry. The same conclusion holds for the number of rolling passes. A second pass gives rise to a much more significant increase in dislocation density than an increase in the asymmetry ratio from 1.5 to 2.

As was found in relation to Fig. 7, where symmetric rolling was studied for different values of the coefficient of rolling friction μ, also Fig. 11 shows the tendency towards a saturation in dislocation density after the second rolling pass. This is most evident at a thickness reduction of 60 %, cf. Fig. 11c.

Note that at 40 and 60 % thickness reduction, cf. Figs. 11b and c, the levels of dis-

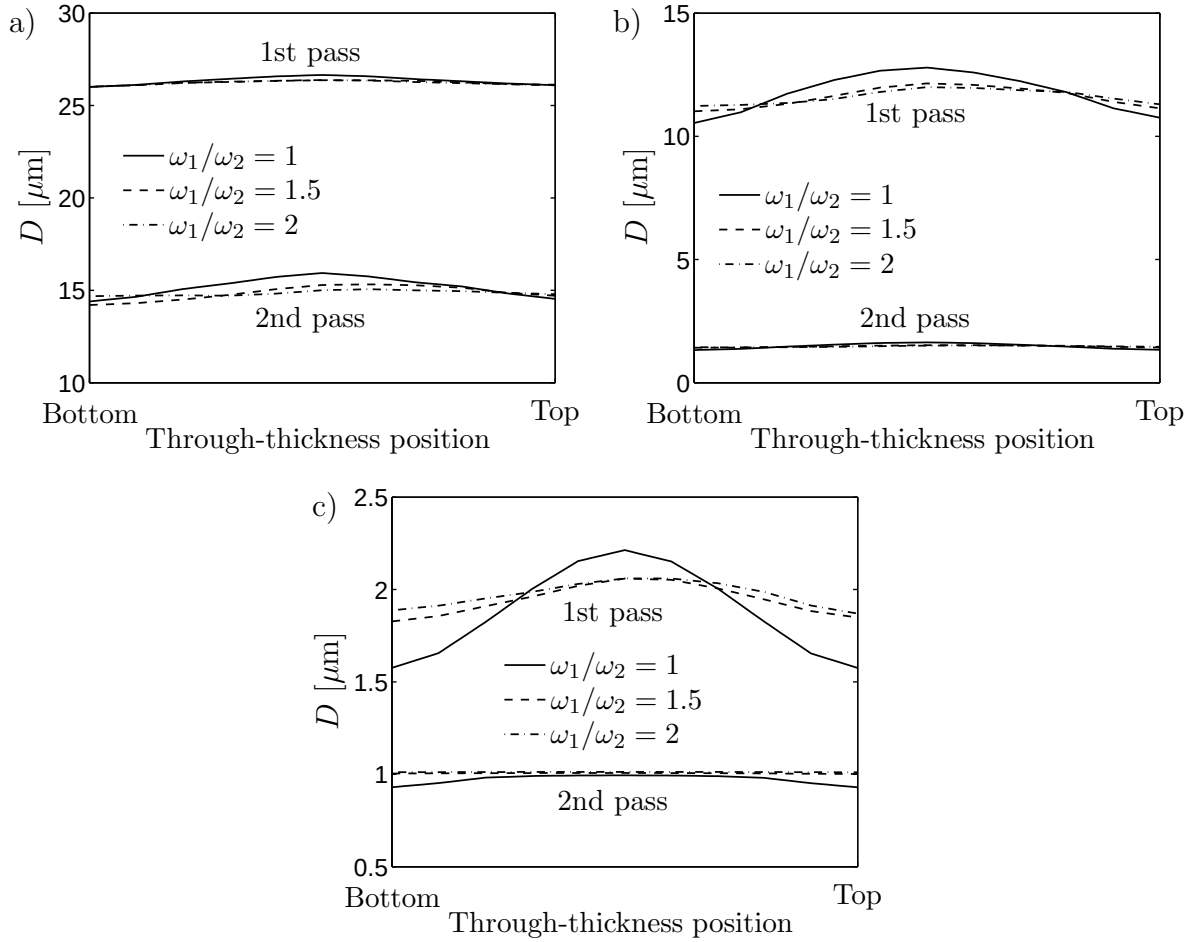

Figure 12: Influence of rolling asymmetry on the through-thickness variation of the average grain size in the sheet after one and two rolling passes, respectively. Results are obtained at thickness reductions (per pass) of: (a) 20 %, (b) 40 % and (c) 60 %.

location density after two passes are almost identical, regardless of the amount of rolling asymmetry. This is again a reflection of the dislocation densities having saturated at this level.

The grain refinement during the simulations of asymmetric rolling processes is shown in Fig. 12. Consistent with the results in Figs. 10 and 11, also the grain refinement is influenced primarily by thickness reduction of the sheet and an additional rolling pass. The impact of rolling asymmetry on grain size reduction is more limited.

At the lowest thickness reduction of 20 %, cf. Fig. 12a, the difference in recrystallized grain size in the presence and in the absence of rolling asymmetry is almost negligible. The effect of asymmetry on grain refinement gradually increases as higher thickness reduction ratios are considered, cf. Figs. 12b and c. This was also observed in asymmetric rolling experiments on AA6111 aluminum in [21]. The experimental results in [21] also show how

the grain size distribution throughout the sheet thickness becomes more even as higher values of asymmetry are used. This is consistent with the appearance of the plots in Fig. 12 becoming more flat as the ratio ω_1/ω_2 is increased.

4.3 Combined effect of increased friction and rolling asymmetry

To investigate their combined effects, variations in both friction and rolling asymmetry are considered simultaneously in this section.

Fig. 13 shows the through-thickness variation of effective plastic strain. Looking at the results at 20 and 40 % thickness reduction in Figs. 13a and b, the cross-section of the sheet is relatively homogeneously exposed to plastic strain. As observed in the previous section,

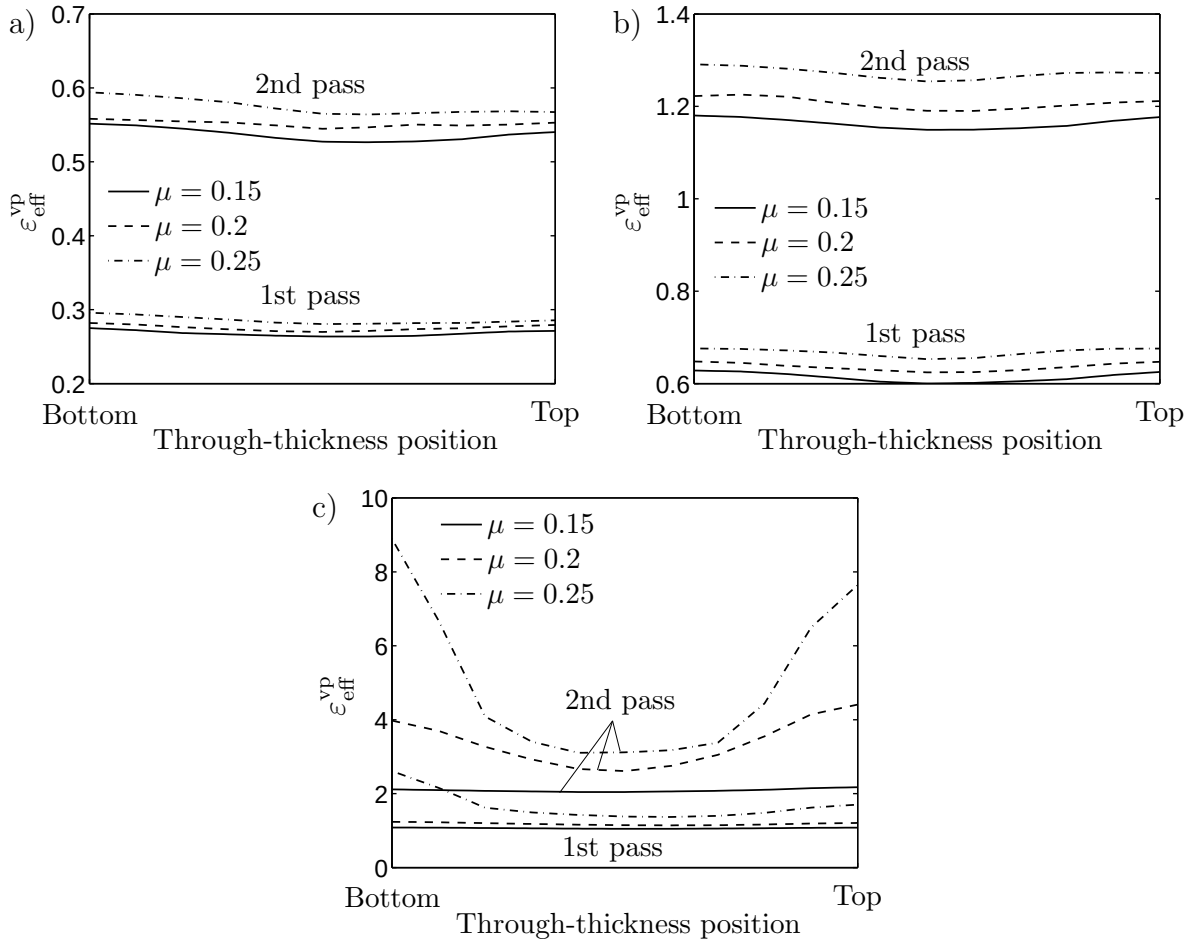

Figure 13: Influence of rolling asymmetry ($\omega_1/\omega_2 = 1.5$) and rolling friction μ on the through-thickness variation of the effective plastic strain in the sheet after one and two rolling passes, respectively. Results are obtained at thickness reductions (per pass) of: (a) 20 %, (b) 40 % and (c) 60 %.

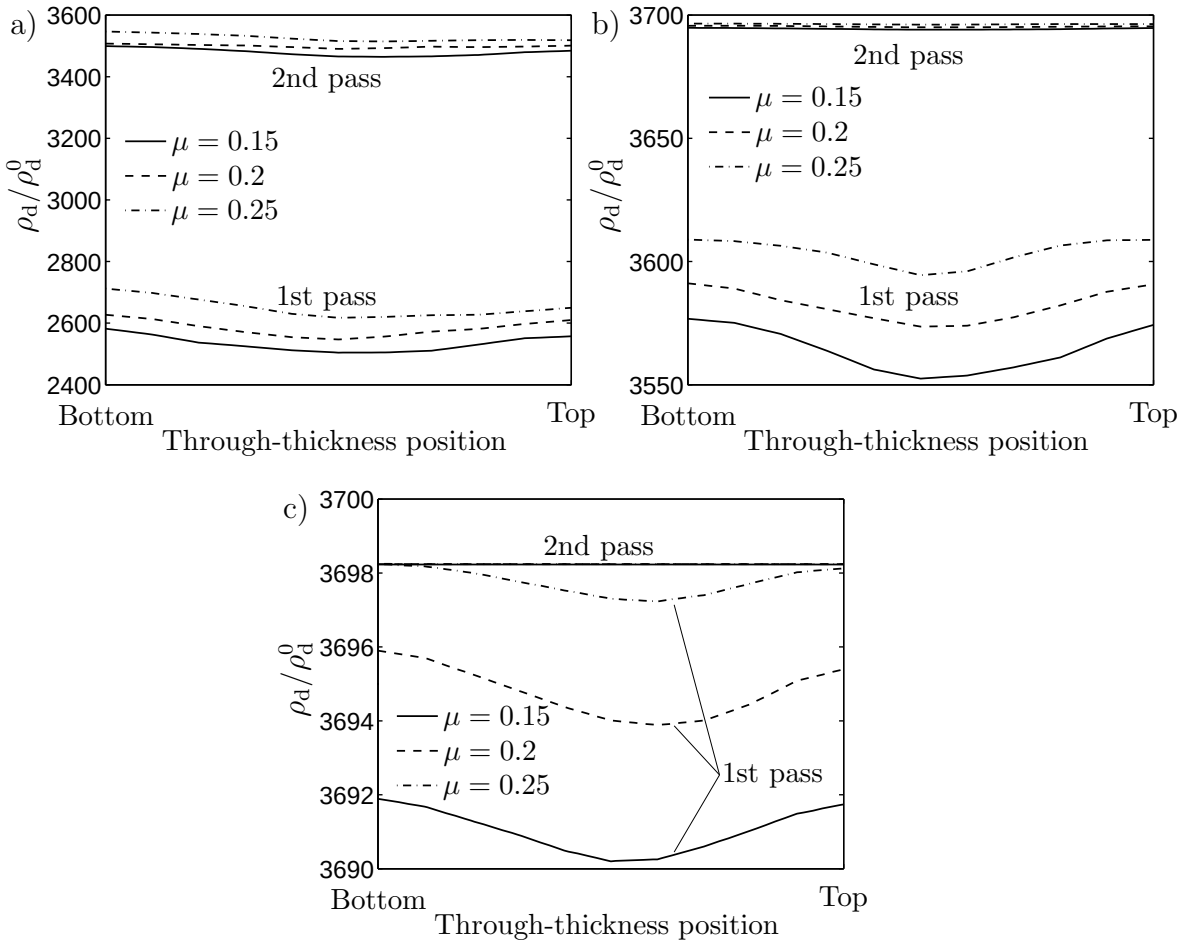

Figure 14: Influence of rolling asymmetry ($\omega_1/\omega_2 = 1.5$) and rolling friction μ on the through-thickness variation of the normalized dislocation density in the sheet after one and two rolling passes, respectively. Results are obtained at thickness reductions (per pass) of: (a) 20 %, (b) 40 % and (c) 60 %.

the absence of large variations through the thickness can be attributed to the asymmetry of the rolling process, also cf. [20]. Higher levels of friction increase the amount of plastic deformation.

At 60 % thickness reduction, cf. Fig. 13c, a different distribution of effective plastic strain is found. After the first pass the distribution is still relatively homogeneous through the thickness whereas after the second pass, the amount of plastic strain near the surfaces of the sheet is greater than in the mid section as the friction is increased. A higher level of friction in combination with the high contact pressure due to significant thickness reduction causes extensive plastic deformation of the sheet, primarily in the top and bottom surface regions.

Similar observations can be made regarding the through-thickness variation of disloca-

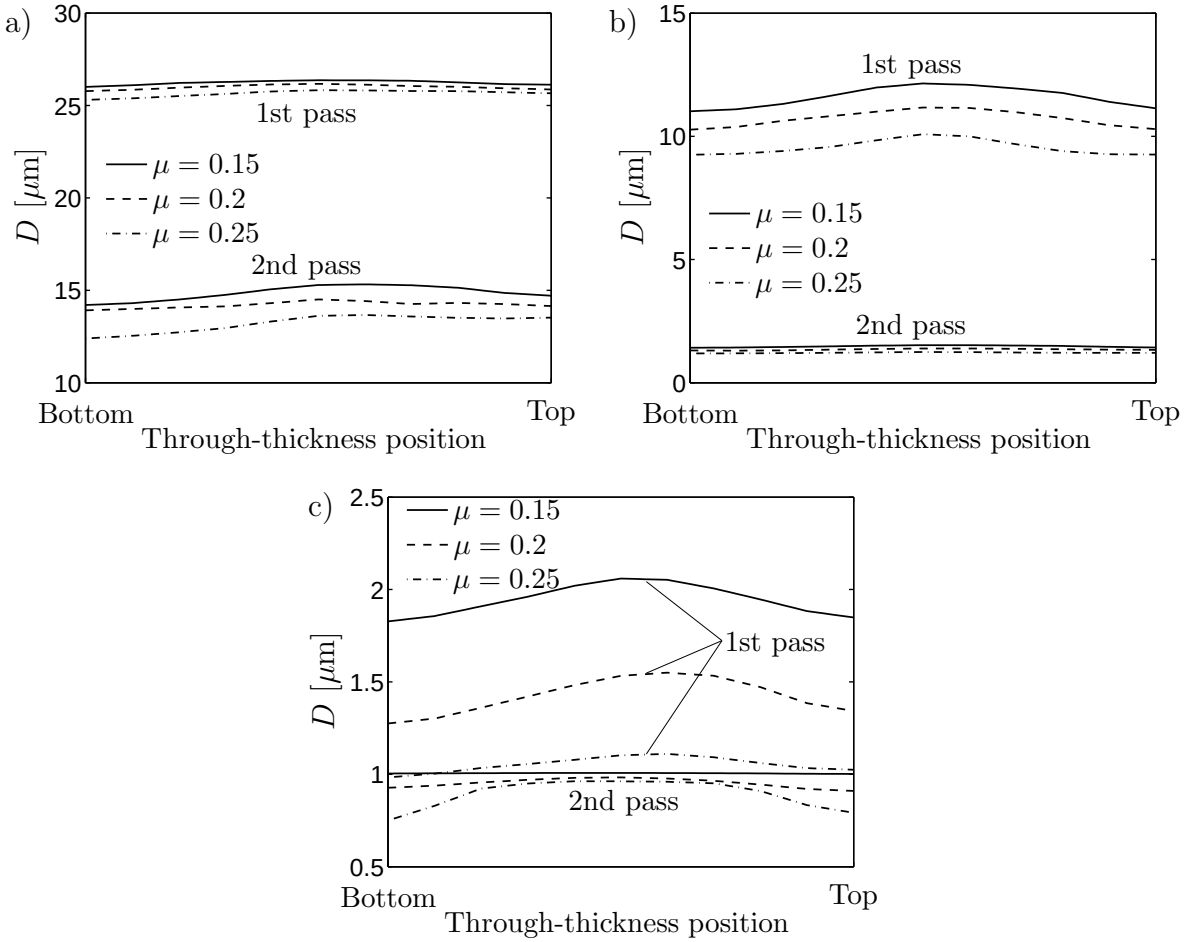

Figure 15: Influence of rolling asymmetry ($\omega_1/\omega_2 = 1.5$) and rolling friction μ on the through-thickness variation of the average grain size in the sheet after one and two rolling passes, respectively. Results are obtained at thickness reductions (per pass) of: (a) 20 %, (b) 40 % and (c) 60 %.

tion density, shown in Fig. 14. At 20 % thickness reduction, cf. Fig. 14a, rolling asymmetry removes much of the variations through the thickness. This effect is, however, gradually removed as 40 and 60 % thickness reduction and one rolling pass is considered, cf. Figs. 14b and c. After two rolling passes, the dislocation density has saturated to a constant level, throughout the thickness of the sheet.

Finally, considering the through-thickness distribution of average grain size shown in Fig. 15, the variations are limited. Again, there is a trend of increasing variation through the thickness with higher thickness reduction ratios. But also at 60 % thickness reduction, cf. Fig. 15c, the variations after two rolling passes are small since the grain size evolves very slowly at the levels of effective plastic strain found here, cf. Fig. 1 and Fig. 13c.

Grain sizes in the order of 1 μm or below are reached for 40 and 60 % thickness reduction

after the second rolling pass for all levels of friction under consideration, cf. Figs. 15b and c. Naturally, involving the most plastic deformation, the situation with 60 % thickness reduction in Fig. 15c yields the smallest grain sizes.

At 60 % thickness reduction, sub-micron grain sizes are reached after the first rolling pass when $\mu = 0.25$ and after the second rolling pass for both $\mu = 0.2$ and $\mu = 0.25$.

5 Concluding remarks

A constitutive model is established, where microstructure parameters such as average grain size and dislocation density are allowed to evolve during plastic deformation of the material. The material model is employed in numerical simulations of cold rolling of AA1050 aluminum sheets, using different processing conditions. Especially the influence of thickness reduction per rolling pass, the influence of friction and the influence of varying degrees of rolling asymmetry on grain refinement and plastic deformation are studied.

The constitutive model used in the present work considers the evolution of the microstructure in terms of dislocation density and grain size and the effect of these quantities on macroscopic material behavior in terms of flow stress and strain rate dependence. Set in a finite strain visco-plastic formulation, the material model provides an efficient tool for simulations of metal forming processes where the effects of dynamic recrystallization and grain size need to be considered.

Results obtained from the numerical simulations in the present work indicate that substantial grain refinement takes place during the rolling process due to dynamic recrystallization and that the extent of the grain refinement can be influenced by varying the process parameters. Since grain size reduction due to dynamic recrystallization is directly related to the magnitude of plastic deformation and accumulation of stored energy in terms of dislocation density, the amount of inelastic deformation of the sheet is a crucial parameter. Increases in rolling friction, thickness reduction per rolling pass and rolling asymmetry are all components in achieving the deformation required for the recrystallization to occur. The simulations further indicate that increased rolling friction and increased thickness reduction are the main components in promoting plastic deformation of the sheet. The degree of rolling asymmetry partakes to a lesser extent. This is in line with experimental results on IF steel presented in [52], where grain refinement is found to primarily take place due to thickness reduction and in second place due to rolling asymmetry.

The asymmetry of the rolling process appears, however, to be an important parameter in obtaining an even distribution of e.g. grain size throughout the thickness of the sheet. Symmetric rolling leads to quite drastic variations in plastic deformation and dislocation accumulation in the through-thickness direction, with the surface regions being most heavily plastically strained. This has a direct impact on the grain refinement due to dynamic recrystallization, resulting in a finer grain structure near the surfaces of the sheet and a

coarser grain structure in the mid region. Introducing rolling asymmetry, plastic deformation and dislocation accumulation is evened out and the resulting grain size is more homogeneously distributed through the thickness. This is in line with experimental results from rolling of AA6111 aluminum in [21] and of AA5754 aluminum in [20].

In the present study, two rolling passes are considered for each setup of process parameters. Naturally, additional passes would cause further plastic deformation of the material, and hence further grain refinement due to dynamic recrystallization. However, the relative influences of rolling friction, thickness reduction and rolling asymmetry found in the present simulations should be indicative of the relative influence of these parameters also after subsequent rolling passes.

References

[1] H. Hallberg, M. Wallin, and M. Ristinmaa. Modeling of discontinuous dynamic recrystallization in pure Cu using a probabilistic cellular automaton. *Comp. Mater. Sci.*, 49(1):25–34, 2010.

[2] H. Jazaeri and F.J. Humphreys. The transition from discontinuous to continuous recrystallization in some aluminum alloys I - the deformed state. *Acta Mater.*, 52:3239–3250, 2004.

[3] H. Jazaeri and F.J. Humphreys. The transition from discontinuous to continuous recrystallization in some aluminum alloys II - annealing behaviour. *Acta Mater.*, 52:3251–3262, 2004.

[4] S. Gourdet and F. Montheillet. An experimental study of the recrystallization mechanism during hot deformation of aluminium. *Mater. Sci. Eng.*, A283:274–288, 2000.

[5] T. Sakai, H. Miura, and X. Yang. Ultrafine grain formation in face centered cubic metals during severe plastic deformation. *Mater. Sci. Eng.*, A499:2–6, 2009.

[6] R.Z. Valiev and T.G. Langdon. Principles of equal-channel angular pressing as a processing tool for grain refinement. *Prog. Mater. Sci.*, 51:881–981, 2006.

[7] J. Jiang, Y. Ding, F. Zuo, and A. Shan. Mechanical properties and microstructures of ultrafine-grained pure aluminum by asymmetric rolling. *Scripta. Mater.*, 60:905–908, 2009.

[8] H. Hallberg, M. Wallin, and M. Ristinmaa. Modeling of continuous dynamic recrystallization in commercial-purity aluminum. *Mater. Sci. Eng.*, A527:1126–1134, 2010.

[9] G. Sachs and L.J. Klinger. The flow of metals through tools of circular contour. *J. Appl. Mech.*, 14:88–98, 1947.

[10] W. Johnson and G. Needham. Further experiments in asymmetrical rolling. *Int. J. Mech. Sci.*, 8:443–455, 1966.

[11] J.-S. Lu, O.-K. Harrer, W. Schwenzfeier, and F.D. Fischer. Analysis of the bending of the rolling material in asymmetrical sheet rolling. *Int. J. Mech. Sci.*, 42:49–61, 2000.

[12] F.A.R. Al-Salehi, T.C. Firbank, and P.R. Lancaster. An experimental determination of the roll pressure distributions in cold rolling. *Int. J. Mech. Sci.*, 15:693–710, 1973.

[13] D. Pan and D.H. Sansome. An experimental study of the effect of roll-speed mismatch on the rolling load during the cold rolling of thin strip. *J. Mech. Work. Technol.*, 6:361–377, 1982.

[14] Y.-M. Hwang and G.-Y. Tzou. Analytical and experimental study on asymmetrical sheet rolling. *Int. J. Mech. Sci.*, 39(3):289–303, 1997.

[15] A.B. Richelsen. Comparison of numerical analysis of rolling with experimental data. *J. Mater. Process. Technol.*, 57:70–78, 1996.

[16] A.B. Richelsen. Elastic-plastic analysis of the stress and strain distributions in asymmetric rolling. *Int. J. Mech. Sci.*, 39(11):1199–1211, 1997.

[17] Z.-C. Lin and C.-C. Shen. A coupled finite element method for a three-dimensional analysis of the flat rolling of aluminum with different reductions. *J. Mater. Process. Technol.*, 110:10–18, 2001.

[18] S.A.A. Akbari Mousavi, S.M. Ebrahimi, and R. Madoliat. Three dimensional numerical analyses of asymmetric rolling. *J. Mater. Process. Technol.*, 187-188:725–729, 2007.

[19] M.O. Ouali and M. Aberkane. Micromechanical modeling of the rolling of a A1050P aluminum sheet. *Int. J. Mater. Forming*, 2:25–36, 2009.

[20] R. Roumina and C.W. Sinclair. Deformation geometry and through-thickness strain gradients in asymmetric rolling. *Metall. Mater. Trans.*, 39A:2495–2503, 2008.

[21] S.-B. Kang, B.-K. Min, H.-W. Kim, D.S. Wilkinson, and J. Kang. Effect of asymmetric rolling on the texture and mechanical properties of AA6111-aluminum sheet. *Metall. Mater. Trans.*, 36A:3141–3149, 2005.

[22] F.J.P. Simoes, R.J.A. de Sousa, J.J.A. Gracio, F. Barlat, and J.W. Yoon. Mechanical behavior of an asymmetrically rolled and annealed 1050-O sheet. *Int. J. Mech. Sci.*, 50:1372–1380, 2008.

[23] K.-H. Kim and D. N. Lee. Analysis of deformation textures of asymmetrically rolled aluminium sheets. *Acta Mater.*, 49:2583–2595, 2001.

[24] H. Jin and D.J. Lloyd. Evolution textures in AA6111 aluminium alloy after asymmetric rolling with various velocity ratios between top and bottom rolls. *Mater. Sci. Eng.*, A465:267–273, 2007.

[25] G. Angella, D. Dellasega, S. Fare, and M. Vedani. A comparison between asymmetric rolling and accumulative roll bonding as means to refine the grain structure of an Al-Mg-Si alloy. *Mater. Sci. Tech.*, 28(1):22–26, 2010.

[26] Q. Cui and K. Ohori. Grain refinement of high purity aluminium by asymmetric rolling. *Mater. Sci. Tech.*, 16(10):1095–1101, 2000.

[27] H. Jin and D.J. Lloyd. The tensile response of a fine-grained AA5754 alloy produced by asymmetric rolling and annealing. *Metall. Mater. Trans.*, 35A:994–1006, 2004.

[28] S.-H. Kim, J.-H. Ryu, K.-H. Kim, and D.-N. Lee. The evolution of shear deformation texture and grain refinement in asymmetrically rolled aluminum sheets. *Mater. Sci. Res. Int.*, 8(1):20–25, 2002.

[29] F. Wang, Q. Zhu, J. Lin, and T.A. Dean. Predicition of microstructural evolution in hot rolling. *J. Mater. Process. Technol.*, 177:530–533, 2006.

[30] M. Toloui and S. Serajzadeh. Modelling recrystallization kinetics during hot rolling of AA5083. *J. Mater. Process. Technol.*, 184:345–353, 2007.

[31] H. Ding, N. Shen, and Y.C. Shin. Predictive modeling of grain refinement during multi-pass cold rolling. *J. Mater. Process. Technol.*, 212:1003–1013, 2012.

[32] Y. Estrin and H.S. Kim. Modelling microstructure evolution toward ultrafine crystallinity produced by severe plastic deformation. *J. Mater. Sci.*, 42:1512–1516, 2007.

[33] S. Poortmans, L. Duchêne, A.M. Habraken, and B. Verlinden. Modelling compression tests on aluminum produced by equal channel angular extrusion. *Acta Mater.*, 57:1821–1830, 2009.

[34] M. Cabibbo, E. Evangelista, and V. Latini. Thermal stability study on two aluminum alloys processed with equal channel angular pressing. *J. Mater. Sci.*, 39:5659–5667, 2004.

[35] S. Poortmans and B. Verlinden. Mechanical properties of fine-grained AA1050 after ECAP. *Mater. Sci. Forum*, 503-504:847–852, 2006.

[36] Y. Estrin and H. Mecking. A unified phenomenological description of work hardening and creep based on one-parameter models. *Acta Metall. Mater.*, 32(1):57–70, 1984.

[37] Y. Estrin. Dislocation theory based constitutive modelling: foundations and applications. *J. Mater. Process. Technol.*, 80-81:33–39, 1998.

[38] J.W. Wyrzykowski and M.W. Grabski. The Hall-Petch relation in aluminum and its dependence on the grain boundary structure. *Phil. Mag. A*, 53(4):505–520, 1986.

[39] E. Kovács-Csetényi, M. Horváth, N.Q. Chinh, and I. Kovács. Effect of grain size on tensile stress and ductility in Al99.99. *Physica Status Solidi*, A166:805–810, 1998.

[40] H. Hasegawa, S. Komura, A. Utsunomiya, Z. Horita, M. Furukawa, M. Nemoto, and T.G. Langdon. Thermal stability of ultrafine-grained aluminum in the presence of Mg and Zr additions. *Mater. Sci. Eng.*, A265:188–196, 1999.

[41] I. Kovács, N.Q. Chinh, and E. Kovács-Csetényi. Grain size dependence of the work hardening process in Al99.99. *Physica Status Solidi*, A194(1):3–18, 2002.

[42] H. Mecking and U.F. Kocks. Kinetics of flow and strain-hardening. *Acta Metall. Mater.*, 29:1865–1875, 1981.

[43] E.P. Busso. A continuum theory for dynamic recrystallization with microstructure-related length scales. *Int. J. Plasticity*, 14(4-5):319–353, 1998.

[44] N. Q. Chinh, G. Hrováth, Z. Horita, and T.G. Langdon. A new constitutive relationship for the homogeneous deformation of metals over a wide range of strain. *Acta Mater.*, 52:3555–3563, 2004.

[45] Q. Wei, S. Cheng, K.T. Ramesh, and E. Ma. Effect of nanocrystalline and ultrafine grain sizes on the strain rate sensitivity and activation volume: fcc versus bcc metals. *Mater. Sci. Eng.*, A381:71–79, 2004.

[46] J. May, H.W. Höppel, and M. Göken. Strain rate sensitivity of ultrafine-grained aluminum processed by severe plastic deformation. *Scripta. Mater.*, 53:189–194, 2005.

[47] H. Miyamoto, K. Ota, and T. Mimaki. Viscous nature of deformation of ultra-fine grain aluminum processed by equal-channel angular pressing. *Scripta Metall. Mater.*, 54:1721–1725, 2006.

[48] J. May, D. Amberger, M. Dinkel, H.W. Höppel, and M. Göken. Monotonic and cyclic deformation behaviour of ultrafine-grained aluminium. *Mater. Sci. Eng.*, A483-484:481–484, 2008.

[49] J. C. Simo. *Handbook of Numerical Analysis*, volume IV, pages 183–499. Elsevier, 1998.

[50] H. Hallberg, K. Ryttberg, and M. Ristinmaa. Model describing material-dependent deformation behavior in high velocity metal forming processes. *ASCE Journal of Engineering Mechanics*, 135(4):345–357, 2009.

[51] H. Gao, S.C. Ramalingam, G.C. Barber, and G. Chen. Analysis of asymmetrical cold rolling with varying coefficients of friction. *J. Mater. Process. Technol.*, 124:178–182, 2002.

[52] A. Wauthier, H. Regle, J. Formigoni, and G. Herman. The effect of asymmetrical cold rolling on kinetics, grain size and texture in IF steels. *Mater. Charact.*, 60:90–95, 2009.